RSC Advances

This is an *Accepted Manuscript*, which has been through the Royal Society of Chemistry peer review process and has been accepted for publication.

Accepted Manuscripts are published online shortly after acceptance, before technical editing, formatting and proof reading. Using this free service, authors can make their results available to the community, in citable form, before we publish the edited article. This *Accepted Manuscript* will be replaced by the edited, formatted and paginated article as soon as this is available.

You can find more information about *Accepted Manuscripts* in the Information for Authors.

Please note that technical editing may introduce minor changes to the text and/or graphics, which may alter content. The journal's standard Terms & Conditions and the Ethical guidelines still apply. In no event shall the Royal Society of Chemistry be held responsible for any errors or omissions in this *Accepted Manuscript* or any consequences arising from the use of any information it contains.

ROYAL SOCIETY OF CHEMISTRY

www.rsc.org/advances

Enhanced Electrochemical Perfomances of Barium Hexaferrite Nanoplates by Zn^{2+} Doping Serving as Anode Material

Chenxi Hu, Song Qiu, Guixia Lu, Huili Cao, Hailong Lv, Shimei Guo and Jiurong Liu,*

Key Laboratory for Liquid–Solid Structural Evolution and Processing of Materials, Ministry of Education and School of Materials Science and Engineering, Shandong University, Jinan, Shandong 250061, China

*** Corresponding Author**

E-mail: jrliu@sdu.edu.cn (J. L.); Tel.: +86-531-88390236 (J. L.)

RSC Advances Accepted Manuscript

ABSTRACT

Zn^{2+}-doped Barium hexaferrite ($BaFe_{12}O_{19}$) nanoplates with ca. 0.4-1.5 μm in diameter and the thickness of ca. 50 nm have been successfully fabricated through a facile hydrothermal approach, followed by an annealing process. The as-prepared Zn^{2+}-doped $BaFe_{12}O_{19}$ nanoplates were first evaluated as anode materials for lithium-ion batteries (LIBs). Electrochemical tests demonstrated that the Zn^{2+}-doped $BaFe_{12}O_{19}$ nanoplates with 2.7 mol% Zn^{2+} doping delivered a higher reversible capacity of 665.5 mAh g^{-1} than that (441.5 mAh g^{-1}) of $BaFe_{12}O_{19}$ nanoplates after 250 cycles at a current density of 100 mA g^{-1}. The superior cycling performances witnessed in Zn^{2+}-doped $BaFe_{12}O_{19}$ are attributed to the Zn^{2+} doping, which can efficiently enhance the electronic conductivity $BaFe_{12}O_{19}$ confirmed by the impedance measurements.

Keywords: Barium hexaferrite; nanoplate; Zn^{2+} doping; electrochemical performance; cycling stability

RSC Advances Accepted Manuscript

1. Introduction

With the increasing energy consumption and environmental deterioration, efficient and environmentally-friendly energy conversion and storage devices have attracted great attention in recent years. Rechargeable lithium-ion batteries (LIBs) have been considered as one of the most competitive energy storage devices due to their high energy density, long life-time, and the sustainable and renewable characteristics. The electrochemical performances of LIBs are largely dependent on their electrode materials. In the past few decades, graphite has been employed as the commercial anode material of LIBs due to its superior electrochemical and structure stability. However, the low theoretical capacity (372 mAh g^{-1}) and poor cycling performance of graphite at high current density have restricted its large-scale application in the ever-growing energy storage devices.[1] Since Tarascon and coworkers[2] firstly reported the conversion reaction mechanism of transition-metal oxides (TMOs) as the LIBs anode materials, researchers have been focusing on exploring alternative TMOs anode materials for their higher theoretical capacities than graphite.[3-6] However, most of transition-metal oxides serving as anodes for LIBs usually suffer from the fast capacity fading and poor cycling performance due to low electrical conductivity and large volume expansion/shrinkage during the lithiation/delithiation processes, which will lead to the destruction of anode structure and rapid degrading of electrochemical performances. A variety of approaches have been employed to improve the reversible capacity and rate capability of transition-metal oxides. Among them, one efficient

RSC Advances Accepted Manuscript

strategy is to design various nanostructures, such as nanoparticles,[7] nanofibers[8] and nanosheets,[9] because nanostructured materials provide better stress-strain relief and maintain the structural integrity of anode materials during the repetitive lithium insertion/extraction processes, and hence enhancing the cycle stability of LIBs. In addition, nanostructured anodes can shorten the pathway for Li-ion diffusion and electron transport as well as provide more contact area with electrolyte, which may facilitate a higher Li-ion flux across the electrode/electrolyte interface leading to higher energy density.[10,11] Another strategy relies mainly on the electrical conductivity improvement of transition-metal oxides. The doping with semiconductor components has been employed to increase the electrical conductivity of electrode materials, which is beneficial to LIBs.[12-14] For example, the boron-doped TiO_2 anode exhibited a higher reversible capacity (166.9 mAh g^{-1}) than that (107.7 mAh g^{-1}) of TiO_2 sample at a current density of 1C,[15] attributing to the increase of interplanar spacing and the decrease of both surface and charge transfer resistance. The Mo^{6+} doped TiO_2 nanoparticles also displayed a significantly lower charge transfer resistance and higher reversible capacity (169.5 mAh g^{-1} after 30 cycles).[16] The Zn^{2+} doped $LiFePO_4$ cathode material exhibited better lithium-ion storage performance comparing with $LiFePO_4$ counterpart due to the expanding of lattice volume and the decrease of charge transfer resistance.[17] The enhanced electrochemical performances were ascribed to the improvements of electron and Li-ion conductivity by the doping of heterogeneous elements.

Recently, nanostructured ternary ferrite (MFe_2O_4) anodes, such as $ZnFe_2O_4$,[18, 19]

RSC Advances Accepted Manuscript

$CoFe_2O_4$,[20] $CuFe_2O_4$[21] and $NiFe_2O_4$[22] have been investigated and exhibited good electrochemical performances due to their high theoretical specific capacities and the feasibility to adjust the working voltage by altering the content of two metal elements.[8, 21] Barium hexaferrites ($BaFe_{12}O_{19}$), an important ferrite, is commonly utilized as magnetic material due to its relatively high Curie temperature, high coercive force and high magnetic anisotropy field, as well as its excellent chemical stability and corrosion resistivity.[23, 24] However, to the best of our knowledge, no investigation has been presented on utilizing barium hexaferrites ($BaFe_{12}O_{19}$) nanoplates as LIBs anode so far.

In this work, the Zn^{2+}-doped $BaFe_{12}O_{19}$ nanoplates were synthesized through a facile hydrothermal route followed by a calcination process. The nanoplates with the thickness of ca. 50 nm will shorten the pathway for Li-ion diffusion and provide more contact surface area between the active materials and electrolyte, and Zn^{2+} doping will increase the electronic conductivity of $BaFe_{12}O_{19}$. Comparing with $BaFe_{12}O_{19}$, the electrochemical measurements demonstrate that the as-prepared Zn^{2+}-doped $BaFe_{12}O_{19}$ nanoplates exhibit superior cycling performances.

2. Experimental

2.1. Materials

Iron nitrate nonahydrate ($Fe(NO_3)_3 \cdot 9H_2O$), barium nitrate ($Ba(NO_3)_2$), zinc nitrate hexahydrate ($Zn(NO_3)_2 \cdot 6H_2O$) and sodium hydroxide (NaOH) were all purchased from Sinopharm Chemical Reagent Co., Ltd. Carbon black, Li foil and Celgard 2300

RSC Advances Accepted Manuscript

were provided by Hefei Kejing Material Technology Co., Ltd, China. Polyvinylidene fluoride (PVDF), $LiPF_6$ (dissolved in ethylene carbonate, dimethyl carbonate, and ethylene methyl carbonate with a volume ratio of 1: 1: 1) were purchased from Shenzhen Biyuan Technology Co., Ltd, China. All chemicals are of analytical grade and were used as received without further purification.

2.2. Fabrication of $BaFe_{12}O_{19}$ and Zn^{2+}-doped $BaFe_{12}O_{19}$ nanoplates

The Zn^{2+}-doped $BaFe_{12}O_{19}$ nanoplates were fabricated by a facile hydrothermal route. Specifically, $Fe(NO_3)_3 \cdot 9H_2O$ (8 mmol), $Ba(NO_3)_2$ (1 mmol) and $Zn(NO_3)_2 \cdot 6H_2O$ (0.25 mmol) were dissolved in 20 mL deionized water, followed by the dropwise addition of 20 mL NaOH (2.2 M) solution under magnetic stirring. The colloid solution was then transformed into a 100 mL Teflon-lined autoclave, and subsequently sealed and heated at 200 ºC for 48 h in an oven. After reaction, the brown precipitate was centrifuged and washed using deionized water for several times, and then dried at 60 ºC in air overnight. As the added amount of NaOH was excessive (the molar ratio of OH^- to all cations was 5:1) to allow all cations (Fe^{3+}, Ba^{2+}, Zn^{2+}) be transformed into the precipitate. Finally, the Zn^{2+}-doped $BaFe_{12}O_{19}$ nanoplates were obtained by annealing the brown precipitate at 900 ºC for 2 h in air. The preparation procedure of $BaFe_{12}O_{19}$ nanoplates was the same as that of Zn^{2+}-doped $BaFe_{12}O_{19}$ only without adding $Zn(NO_3)_2 \cdot 6H_2O$ in the first step.

2.3.Characterizations

The structure of products was determined by X-ray powder diffraction (XRD) on a

RSC Advances Accepted Manuscript

Rigaku D/Max-RC X-ray diffractometer with Ni filtered Cu Kα radiation (λ = 0.1542 nm, V = 40 kV, I = 40 mA) in the range of 10-80° at a scanning rate of 4° min^{-1}. The morphologies of the samples were examined by using a JSM-6700F field emission scanning electron microscopy (FE-SEM) at an accelerating voltage of 20 kV and an electric current of 1.0×10^{-10} A, and a JEOL JEM-2100 high-resolution transmission electron microscopy (HR-TEM) with an accelerating voltage of 200 kV. X-ray photoelectron spectroscopy (XPS) was recorded on a Kratos Analytical spectrometer, using Al Kα (hv = 1486.6 eV) radiation as the excitation source, under a condition of anode voltage of 12 kV and an emission current of 10 mA.

2.4. Electrochemical measurements

To prepare the working electrode, the active material, carbon black, and polyvinylidene fluoride (PVDF) with a weight ratio of 8:1:1 were mixed in N-methyl-2-pyrrolidinone (NMP) to form a homogenous slurry, which was coated on a copper foil substrate, followed by drying in a vacuum oven at 120 ºC for 12 h. The CR2025-type cells were assembled using Li foil as counter and reference electrode, Celgard 2300 as separator, and 1 M $LiPF_6$ (dissolved in ethylene carbonate, dimethyl carbonate, and ethylene methyl carbonate with a volume ratio of 1:1:1) as electrolyte. The assembly was performed in a glove box filled with argon atmosphere. The performance of the cells was evaluated galvanostatically in the voltage range from 0.02 to 3 V at certain current densities on a LAND CT2001A battery test system. Cyclic voltammogram (CV) was obtained on a IviumStat electrochemistry workstation with a scanning rate of 0.3 mV s^{-1} and the potential *vs*. Li^+/Li ranging

RSC Advances Accepted Manuscript

from 0.01 to 3 V. The electrochemical impedance spectra were obtained on the same instrument with AC signal amplitude of 10 mV in the frequency range from 100 kHz to 0.01 Hz. The data were adopted to draw Nyquist plots using real part Z' as X axis, and imaginary part Z'' as Y axis.

3. Results and discussion

3.1. Characterizations of Zn^{2+}-doped $BaFe_{12}O_{19}$ nanoplates

As shown in Fig. 1a, XRD pattern confirms that all diffraction peaks of the product synthesized by combining the facile hydrothermal approach with a calcination process match well with those of hexagonal-structured $BaFe_{12}O_{19}$ (JCPDS No. 39-1433), and no other peaks are detected, confirming the high purity of $BaFe_{12}O_{19}$. For comparison, Fig. 1b indicates that the diffraction pattern of Zn^{2+}-doped $BaFe_{12}O_{19}$ is similar to that of $BaFe_{12}O_{19}$ sample. However, from the enlarged (114) peak (insert of Fig. 1), a slight peak shift to lower angle, which demonstrates the Zn^{2+} doping into crystalline lattice of $BaFe_{12}O_{19}$, is detected. The similar phenomenon has also been found in our previous research.[25] To further illustrate the variation of crystal structure, the diffraction data of (114) plane is used to calculate the lattice constant. With the Zn^{2+} doping, the calculated lattice distance between (114) planes by the Braggs law changes from 0.2623 to 0.2633 nm according to the peak shift angle.[26]

The morphology of the products was examined by the field emission scanning electron microscope (FE-SEM). As shown in Fig. 2a, large-scale $BaFe_{12}O_{19}$ nanoplates with ca. 1.0-2.5 μm in diameter and the thickness of ca. 50 nm have been

RSC Advances Accepted Manuscript

synthesized through a facile hydrothermal route followed by a calcination process. The high magnification image shows that the synthesized $BaFe_{12}O_{19}$ nanoplates have hexagonal structure (Fig. 2c&e). With the Zn^{2+} doping, there is no obvious variation on the morphology of the as-synthesized Zn^{2+}-doped $BaFe_{12}O_{19}$ (Fig. 2b), but the size of nanoplates decreased to ca. 0.4-1.5 μm (Fig. 2d&f), which is smaller than that of $BaFe_{12}O_{19}$ nanoplates. The histogram of particle diameter distribution given in Fig. S1a also showed that, although there was a wide diameter distribution, the Zn^{2+}-doped $BaFe_{12}O_{19}$ sample had smaller average diameter than $BaFe_{12}O_{19}$. Meanwhile, the thickness of both samples had no obvious variation from the statistical size in Fig. S1b. Previous investigations also confirm that the heterogeneous element doping will inhibit the growth of oxide grains.[16, 27] The elemental maps of Zn^{2+}-doped $BaFe_{12}O_{19}$ samples are shown in Fig. 3. From the selected area on one nanoplate in SEM image, a uniform distribution of Fe, Ba, Zn and O elements can be found, also suggesting the Zn^{2+} doping into the crystalline lattice of $BaFe_{12}O_{19}$. As the added amount of NaOH was much excessive and the XRD analysis showed that no other obvious diffraction peaks were detected, we can speculate that Zn^{2+} doping amount in the synthesized Zn^{2+}-doped $BaFe_{12}O_{19}$ nanoplates is 2.7 mol% according to the addition molar ratio of reactants. Meanwhile, although the EDX analysis showed in Fig. S2 and Table S1 of supporting information is not accurate to measure the Zn^{2+} doping amount, the molar ratio of Zn^{2+} is 3.1 mol% calculated from the EDX data (Zn^{2+}: Ba^{2+}: Fe^{3+} =0.55: 1.66: 15.22), which is close to 2.7 mol%, also suggesting the complete precipitation of Zn^{2+}. In the TEM image of Zn^{2+}-doped $BaFe_{12}O_{19}$ nanoplates (Fig. 4a), the diameter of

RSC Advances Accepted Manuscript

nanoplates is ca. 0.4-1.0 μm, consistent with the SEM observation as shown in Fig. 2b,d&f. From the higher resolution image (Fig. 4b), the measured lattice spacing is 0.441 nm, corresponding to the (102) crystal plane of hexagonal $BaFe_{12}O_{19}$. The HR-TEM measurement reveals the single crystalline nature of the nanoplates.

X-ray photoelectron spectroscopy (XPS) analysis was carried out to determine the composition and chemical bonding of $BaFe_{12}O_{19}$ and Zn^{2+}-doped $BaFe_{12}O_{19}$ nanoplates. From the survey scan spectra (Fig. 5a), the peaks of Fe 2p, Ba 3d, and O 1s were detected in both samples indicating the existence of Fe, Ba, and O elements, while the Zn 2p peaks were only found in Zn^{2+}-doped $BaFe_{12}O_{19}$ sample. The C 1s peak in both samples results from a small amount of carbon contamination due to the ambient exposure of samples, which is consistent with previous research.[28] Two peaks at the binding energy of 779.7 and 795.0 eV (Fig. 5b) are assigned to Ba $3d_{5/2}$ and Ba $3d_{3/2}$, respectively. Previous investigation indicated that the Ba $3d_{5/2}$ and Ba $3d_{3/2}$ XPS peaks of BaO were observed at the binding energy of 779.65 and 795.00 eV,[27] respectively, confirming that the Ba state in two samples is Ba^{2+}. The Fe $2p_{3/2}$ and Fe $2p_{1/2}$ peaks are observed at 710.7 and 724.3 eV (Fig. 5c), respectively. The fingerprint shakeup satellite peak of Fe_2O_3 at ca. 719 eV is observed, suggesting that the valence of Fe in two samples is Fe^{3+}.[29] As shown in Fig. 5d, the Zn $2p_{3/2}$ and Zn $2p_{1/2}$ peaks at 1021.2 and 1044.3 eV, which was only detected in the Zn^{2+}-doped $BaFe_{12}O_{19}$ sample, further confirmed the Zn^{2+} doping into $BaFe_{12}O_{19}$ nanoplates.

3.2 Electrochemical Performances of Zn^{2+}-doped $BaFe_{12}O_{19}$ nanoplates

In order to evaluate the cycle performances of the electrodes, the discharge/charge

RSC Advances Accepted Manuscript

measurements were evaluated by LAND CT2001A battery test system at a current density of 100 mA g^{-1}. Fig. 6a and 6b shows the selected discharge/charge curves of $BaFe_{12}O_{19}$ and Zn^{2+}-doped $BaFe_{12}O_{19}$ nanoplates, respectively. In the cathodic reaction process, the first discharge curve of $BaFe_{12}O_{19}$ (Fig. 6a) reveals a decrease to 0.73 V, corresponding to the Li-ion insertion into $BaFe_{12}O_{19}$.[30] A well-defined potential plateau at ca. 0.73 V suggests the reduction of Ba^{2+} and Fe^{3+} to their metallic state and the formation of amorphous Li_2O, while the first charge curve shows no apparent plateau but a slope from 1.3 to 1.9 V, suggesting the oxidation of the metallic iron and barium into Ba^{2+} and Fe^{3+}. When the first cycle is finished, the cell exhibits the initial discharge and charge capacities of 806.8 and 401.2 mAh g^{-1}, respectively, corresponding to the initial coulombic efficiency (the ratio of charge capacity to discharge capacity) of only 49.7%. The large capacity loss can be attributed to the lithium insertion into irreversible sites and the irreversible lithium loss due to the formation of solid electrolyte interface (SEI) layer during the first discharge/charge process.[31-33] For the Zn^{2+}-doped $BaFe_{12}O_{19}$ sample, as shown in Figure 6b, the potential/capacity profiles display the similar variation tendencies to those of pure $BaFe_{12}O_{19}$. In the first discharge curve, the initial discharge capacity is 885.1 mAh g^{-1} with the voltage decreasing to 0.02 V. When the first charge was completed, a specific capacity of 525.0 mAh g^{-1} was obtained, and the initial coulombic efficiency was 59.3%, which is obviously higher than that of $BaFe_{12}O_{19}$ sample (49.7%), indicating that Zn^{2+} doping not only enhanced the specific capacity of $BaFe_{12}O_{19}$ but also the initial coulombic efficiency probably due to the improvement of electronic

RSC Advances Accepted Manuscript

conductivity. The CV profiles for the initial three cycles of $BaFe_{12}O_{19}$ and Zn^{2+}-doped $BaFe_{12}O_{19}$ nanoplates are shown in Fig. 6c and 6d, respectively. As shown in the Fig. 6c, during the first cathodic scan, a wide peak from 0.3 to 0.75 V might be attributed to the reduction of Ba^{2+} and Fe^{3+} to their metallic state and the formation of amorphous Li_2O, the anodic peak at around 1.75 V can be attributed to the oxidation of the metallic iron and barium into Ba^{2+} and Fe^{3+}.[34-36] Fig. 6d shows a similar profile, the cathodic peak is located at ca. 0.5 V in the first cycle and the anodic peak is at ca. 1.6 V, suggesting the similar oxidation and reduction processes. From the second cycle, the cathodic peak becomes weak and broad, and the cathodic and anodic peaks shift to higher voltage, which can be attributed to the polarization of the active material in the first cycle.[37, 38]

The cycling performances of both samples are depicted in Fig. 7. It can be found that the Zn^{2+}-doped $BaFe_{12}O_{19}$ anode delivers the reversible capacity of 665.5 mAh g^{-1} after 250 cycles at the current density of 100 mA g^{-1}. The specifical capacity decreases gradually to ca. 300 mAh g^{-1} in the initial 12 cycles attributing to the extra consumption of lithium during the formation of SEI layer and the irreversible conversion reaction.[39, 40] After 12 cycles, the reversible capacity of Zn^{2+}-doped $BaFe_{12}O_{19}$ anode exhibited an increasing tendency with the cycling onward, even reached 665.5 mAh g^{-1} after 250 cycles due to the gradual activation of anode made of metal oxide nanomaterials during the discharge/charge processes.[41-43] The coulombic efficiency of Zn^{2+}-doped $BaFe_{12}O_{19}$ anode quickly reaches to 90% in the second cycle, and remains above 99% after 10 cycles. In comparison, the $BaFe_{12}O_{19}$ anode shows

RSC Advances Accepted Manuscript

the similar variation tendency of reversible capacity with cycling and only delivers the reversible capacity of 441.5 mAh g^{-1} after 250 cycles, which is much lower than that (665.5 mAh g^{-1}) of Zn^{2+}-doped $BaFe_{12}O_{19}$ nanoplates. The higher capacity retention of Zn^{2+}-doped $BaFe_{12}O_{19}$ nanoplates than that of $BaFe_{12}O_{19}$ at each cycle demonstrates that Zn^{2+} doping significantly improves the cycling performance and leads to higher reversible capacity.

Fig. 8 shows the rate performance of $BaFe_{12}O_{19}$ and Zn^{2+}-doped $BaFe_{12}O_{19}$ nanoplates evaluated at different current densities after 100 cycles. The Zn^{2+}-doped $BaFe_{12}O_{19}$ product delivers reversible capacities of 325.2, 260.8, 162.9, 65.3 mAh g^{-1} at the current densities of 200, 400, 800 and 1600 mA g^{-1}, respectively. When the current density is returned to 100 mA g^{-1}, the discharge capacity is ca. 380.4 mAh g^{-1}. The $BaFe_{12}O_{19}$ nanoplates only deliver the reversible capacities of 163.6, 110.2, 68.7, 33.3 mAh g^{-1} at the current densities of 200, 400, 800 and 1600 mA g^{-1}, respectively. When the current density is returned to 100 mA g^{-1}, the discharge capacity is ca. 203.4 mAh g^{-1}. Apparently, the Zn^{2+} doped $BaFe_{12}O_{19}$ nanoplates exhibit much higher capacities than the sample without Zn^{2+} doping at the same current density, demonstrating that Zn^{2+} doping can effectively promote the rate performance.

To further clarify the effects of Zn^{2+} doping on the electrochemical performance, the electrochemical impedance spectroscopy (EIS) measurement was conducted to reveal the lithium ion diffusion and electron transfer. As shown in Fig. 9, the Nyquist plots exhibit a semicircle in the high frequency region and an oblique line in the low frequency region. The diameter of semicircle is in direct proportion to the impedance,

RSC Advances Accepted Manuscript

while the slope of the oblique line at low frequency corresponds to the Warburg impedance associated with the Li-ion diffusion.[44, 45] Before the discharge/charge process, the measured resistance values for Zn^{2+}-doped $BaFe_{12}O_{19}$ and $BaFe_{12}O_{19}$ anode are ca. 119 and 260 Ω, respectively (Fig. 9a). Apparently, the resistance value of Zn^{2+}-doped $BaFe_{12}O_{19}$ is much smaller than that of $BaFe_{12}O_{19}$, indicating that Zn^{2+} doping indeed enhanced the electronic conductivity and charge transfer of $BaFe_{12}O_{19}$.[46, 47] Moreover, the Zn^{2+}-doped $BaFe_{12}O_{19}$ and $BaFe_{12}O_{19}$ anodes exhibit almost the same slope for the oblique lines at low frequency, suggesting that there are no obvious differences on the lithium ion diffusion in both samples before cycling. Fig. 9b shows the Nyquist plots of both cells measured after 250 cycling. The measured resistance value is 77 Ω for Zn^{2+}-doped $BaFe_{12}O_{19}$ anode, which is lower than that of $BaFe_{12}O_{19}$ (137 Ω), attributing to the conductivity improvement caused by Zn^{2+} doping. It is worth noted that, comparing with the resistance values measured before discharge/charge process, both Zn^{2+}-doped $BaFe_{12}O_{19}$ and $BaFe_{12}O_{19}$ anodes display the decrease of resistance values after 250 cycling, which results in the reversible capacity increase with cycling due to the gradual activation of the anode materials (Fig.7).[43] Combining the electrochemical performances with the structure characterization, the Zn^{2+}-doped $BaFe_{12}O_{19}$ nanoplates exhibit higher reversible capacity (665.5 mAh g^{-1}) than $BaFe_{12}O_{19}$ nanoplates (441.5 mAh g^{-1}) after 250 cycles although there is no obvious variation on the morphology and structure of two products. The impedance measurements indicate that the Zn^{2+}-doping is beneficial to increase the electronic conductivity of $BaFe_{12}O_{19}$, finally improving the cycling

RSC Advances Accepted Manuscript

performance.

4. Conclusions

In summary, $BaFe_{12}O_{19}$ and Zn^{2+}-doped $BaFe_{12}O_{19}$ nanoplates have been synthesized by a facile approach. As anode material for Li-ion battery, the Zn^{2+}-doped $BaFe_{12}O_{19}$ nanoplates exhibited more superior cycling performance comparing with $BaFe_{12}O_{19}$. The as-prepared nanoplates with the thickness of ca. 50 nm provide large contact surface area between the active material and electrolyte, and Zn^{2+} doping increases the electronic conductivity of $BaFe_{12}O_{19}$. Therefore, the researches on the Zn^{2+}-doped $BaFe_{12}O_{19}$ nanoplates demonstrated an efficient way to enhance the electronic conductivity of metallic oxides, and thereby realize the improvement of electrochemical performances.

Acknowledgements

This work was supported by the Fundamental Research Funds of Shandong University (2015JC016). The authors also acknowledge the financial supports from the Doctoral Program of Higher Education of China (20130131110068), and Natural Science Fund for Distinguished Young Scholars of Shandong (JQ201312).

RSC Advances Accepted Manuscript

References:

1. X. Wang, Y. Wang, L. Yang, K. Wang, X. Lou and B. Cai, *J Power Sources*, 2014, **262**, 72-78.
2. P. Poizot, S. Laruelle, S. Grugeon, L. Dupont and J. M. Tarascon, *Nature*, 2000, **407**, 496-499.
3. D. Wang, Y. Yu, H. He, J. Wang, W. Zhou and H. D. Abruna, *ACS nano*, 2015, **9**, 1775-1781.
4. X. Wang, H. Guan, S. Chen, H. Li, T. Zhai, D. Tang, Y. Bando and D. Golberg, *Chem Commun*, 2011, **47**, 12280-12282.
5. D. Su, H. Kim, W. Kim and G. Wang, *Chem-Eur J*, 2012, **18**, 8224-8229.
6. J. S. Chen, T. Zhu, X. H. Yang, H. G. Yang and X. W. Lou, *J Am Chem Soc*, 2010, **132**, 13162-13164.
7. P. Kubiak, M. Pfanzelt, J. Geserick, U. Hoermann, N. Huesing, U. Kaiser and M. Wohlfahrt-Mehrens, *J Power Sources*, 2009, **194**, 1099-1104.
8. P. F. Teh, Y. Sharma, S. S. Pramana and M. Srinivasan, *J Mater Chem*, 2011, **21**, 14999-15008.
9. L. Ren, Y. Liu, X. Qi, K. S. Hui, K. N. Hui, Z. Huang, J. Li, K. Huang and J. Zhong, *J Mater Chem*, 2012, **22**, 21513-21518.
10. Y. Zhang, F. Du, X. Yan, Y. Jin, K. Zhu, X. Wang, H. Li, G. Chen, C. Wang and Y. Wei, *ACS APPLIED MATERIALS & INTERFACES*, 2014, **6**, 4458-4465.
11. J. Luo, X. Xia, Y. Luo, C. Guan, J. Liu, X. Qi, C. F. Ng, T. Yu, H. Zhang and H. J. Fan, *ADVANCED ENERGY MATERIALS*, 2013, **3**, 737-743.
12. D. Pasero, N. Reeves and A. R. West, *J Power Sources*, 2005, **141**, 156-158.
13. Y. J. Mai, J. P. Tu, X. H. Xia, C. D. Gu and X. L. Wang, *J Power Sources*, 2011, **196**, 6388-6393.
14. H. Liu, Q. Cao, L. J. Fu, C. Li, Y. P. Wu and H. Q. Wu, *Electrochem Commun*, 2006, **8**, 1553-1557.
15. J. Jeong, D. Jung, E. W. Shin and E. Oh, *J Alloy Compd*, 2014, **604**, 226-232.
16. V. T. Trang, A. K. Rai, J. Gim, S. Kim and J. Kim, *J Alloy Compd*, 2014, **598**, 16-22.
17. Y. P. Wu, H. Liu, Q. Cao, L. J. Fu, C. Li and H. Q. Wu, *Electrochem Commun*, 2006, **8**, 1553-1557.
18. Z. Xing, Z. Ju, J. Yang, H. Xu and Y. Qian, *NANO RESEARCH*, 2012, **5**, 477-485.
19. X. Guo, X. Lu, X. Fang, Y. Mao, Z. Wang, L. Chen, X. Xu, H. Yang and Y. Liu, *Electrochem Commun*, 2010, **12**, 847-850.
20. S. Li, B. Wang, J. Liu and M. Yu, *Electrochim Acta*, 2014, **129**, 33-39.
21. Z. Xing, Z. Ju, J. Yang, H. Xu and Y. Qian, *Electrochim Acta*, 2013, **102**, 51-57.
22. Y. Ding, Y. Yang and H. Shao, *J Power Sources*, 2013, **244**, 610-613.
23. J. G. Huang, H. R. Zhuang and W. L. Li, *Mater Res Bull*, 2003, **38**, 149-159.
24. A. Mali and A. Ataie, *Scripta Mater*, 2005, **53**, 1065-1070.
25. G. Lu, S. Qiu, J. Liu, X. Wang, C. He and Y. Bai, *Electrochim Acta*, 2014, **117**, 230-238.
26. J. Liu, Y. Bin and M. Matsuo, *JOURNAL OF PHYSICAL CHEMISTRY C*, 2012, **116**, 134-143.
27. L. Wang, J. Zhang, Q. Zhang, N. Xu and J. Song, *J Magn Magn Mater*, 2015, **377**, 362-367.
28. J. Liu, Y. Mao, E. Lan, D. R. Banatao, G. J. Forse, J. Lu, H. Blom, T. O. Yeates, B. Dunn and J. P. Chang, *J Am Chem Soc*, 2008, **130**, 16908-16913.
29. T. Fujii, F. de Groot, G. A. Sawatzky, F. C. Voogt, T. Hibma and K. Okada, *Phys Rev B*, 1999, **59**, 3195-3202.
30. Q. Zhang, Z. Shi, Y. Deng, J. Zheng, G. Liu and G. Chen, *J Power Sources*, 2012, **197**, 305-309.
31. K. Zhang, P. Han, L. Gu, L. Zhang, Z. Liu, Q. Kong, C. Zhang, S. Dong, Z. Zhang, J. Yao, H. Xu,

RSC Advances Accepted Manuscript

G. Cui and L. Chen, *ACS APPLIED MATERIALS & INTERFACES*, 2012, **4**, 658-664.

32. Y. J. Mai, D. Zhang, Y. Q. Qiao, C. D. Gu, X. L. Wang and J. P. Tu, *J Power Sources*, 2012, **216**, 201-207.

33. Z. Cui, X. Guo and H. Li, *Electrochim Acta*, 2013, **89**, 229-238.

34. Y. Zhao, Y. Huang, Q. Wang, Y. Wang and M. Zong, *J Sol-Gel Sci Techn*, 2013, **66**, 238-241.

35. Y. Yang, Y. Zhao, L. Xiao and L. Zhang, *Electrochem Commun*, 2008, **10**, 1117-1120.

36. F. M. Courtel, Y. Abu-Lebdeh and I. J. Davidson, *Electrochim Acta*, 2012, **71**, 123-127.

37. Y. Deng, Q. Zhang, Z. Shi, L. Han, F. Peng and G. Chen, *Electrochim Acta*, 2012, **76**, 495-503.

38. J. Wang, C. Zhong, D. Wexler, N. H. Idris, Z. Wang, L. Chen and H. Liu, *Chem-Eur J*, 2011, **17**, 661-667.

39. E. Zhang, Z. Xing, J. Wang, Z. Ju and Y. Qian, *RSC ADVANCES*, 2012, **2**, 6748-6751.

40. H. Shim, I. Cho, K. S. Hong, A. Lim and D. Kim, *JOURNAL OF PHYSICAL CHEMISTRY C*, 2011, **115**, 16228-16233.

41. X. Zhang, H. Chen, Y. Xie and J. Guo, *JOURNAL OF MATERIALS CHEMISTRY A*, 2014, **2**, 3912-3918.

42. Z. Wang, D. Luan, S. Madhavi, Y. Hu and X. W. D. Lou, *ENERGY & ENVIRONMENTAL SCIENCE*, 2012, **5**, 5252-5256.

43. X. Gu, L. Chen, Z. Ju, H. Xu, J. Yang and Y. Qian, *Adv Funct Mater*, 2013, **23**, 4049-4056.

44. G. Zhou, D. Wang, F. Li, L. Zhang, N. Li, Z. Wu, L. Wen, G. Q. M. Lu and H. Cheng, *Chem Mater*, 2010, **22**, 5306-5313.

45. V. Freger, *Electrochem Commun*, 2005, **7**, 957-961.

46. H. Fang, H. Yi, C. Hu, B. Yang, Y. Yao, W. Ma and Y. Dai, *Electrochim Acta*, 2012, **71**, 266-269.

47. H. Liu, Q. Cao, L. J. Fu, C. Li, Y. P. Wu and H. Q. Wu, *Electrochem Commun*, 2006, **8**, 1553-1557.

RSC Advances Accepted Manuscript

Fig. 1. XRD pattern of standard BaFe12O19 (a) and Zn2+-doped BaFe12O19 (b). The inset is the highlighted (114) peak of BaFe12O19 and Zn2+-doped BaFe12O19.

Fig. 2. SEM images of BaFe12O19 (a, c,e) and Zn2+-doped BaFe12O19 (b, d,f) nanoplates.

Fig. 3. SEM and EDX mapping images (Fe, O, Ba, Zn) of Zn2+-doped BaFe12O19 nanoplates.

Fig. 4. HR-TEM images of Zn2+-doped BaFe12O19 nanoplates at different magnifications (a, b).

Fig. 5. XPS spectra of (a) survey-scan, (b) Ba 3d, (c) Fe 2p, and (d) Zn 2p of BaFe12O19 and Zn2+-doped BaFe12O19 nanoplates.

Fig. 6. Galvanostatic discharge/charge curves of the 1st, 2nd, 150th, and 250th cycle for (a) BaFe12O19 and (b) Zn2+-doped BaFe12O19 nanoplates. Cyclic volta voltammograms at a scanning rate of 0.3 mV s-1 between 0.1 and 3.0 V for (c) BaFe12O19 and (d) Zn2+-doped BaFe12O19 nanoplates.

Fig. 7. Cycling performance of BaFe12O19 and Zn2+-doped BaFe12O19 nanoplates at a current density of 100 mA g-1, and columbic efficiency of Zn2+-doped BaFe12O19 nanoplates

Fig. 8. Discharge and charge capacities of Zn2+-doped BaFe12O19 and BaFe12O19 nanoplates at different cycling rates (from 100 to 1600 mA g-1).

Fig. 9. Nyquist plots of BaFe12O19 and Zn2+-doped BaFe12O19 anodes (a) before discharge/charge process and (b) after 250 cycles.

RSC Advances Accepted Manuscript

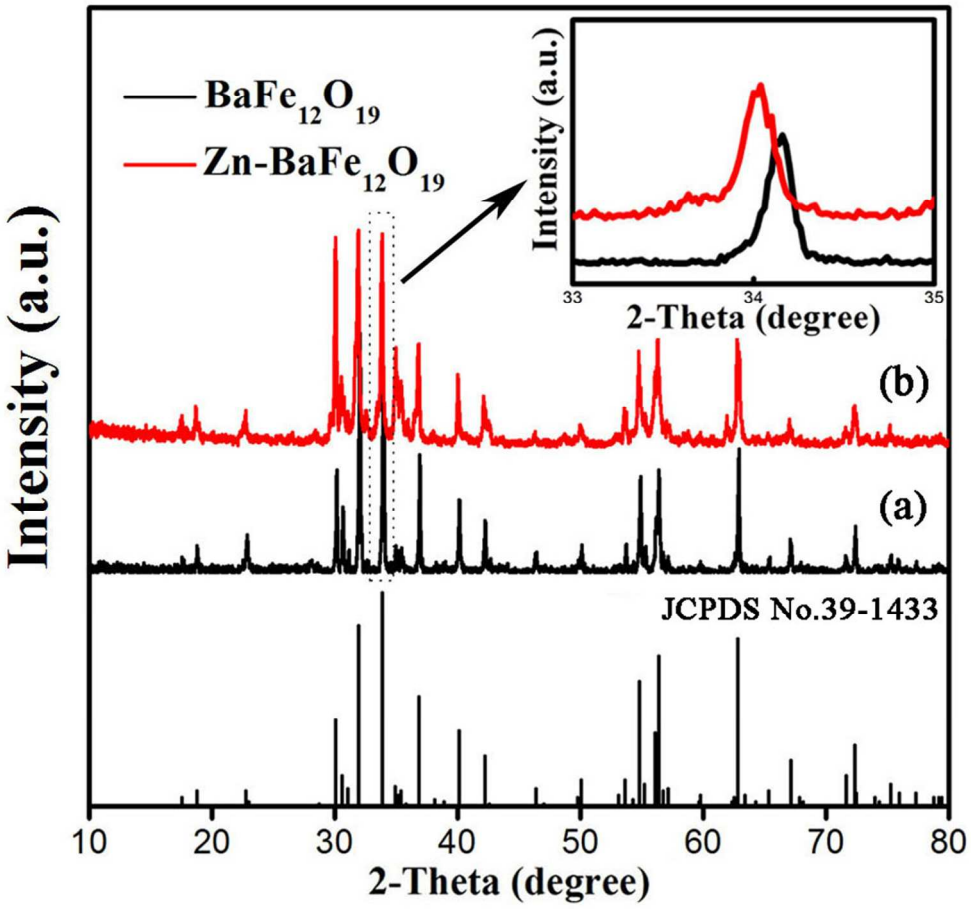

Fig. 1. XRD pattern of standard BaFe12O19 (a) and Zn2+-doped BaFe12O19 (b). The inset is the highlighted (114) peak of BaFe12O19 and Zn2+-doped BaFe12O19.
99x92mm (300 x 300 DPI)

RSC Advances Accepted Manuscript

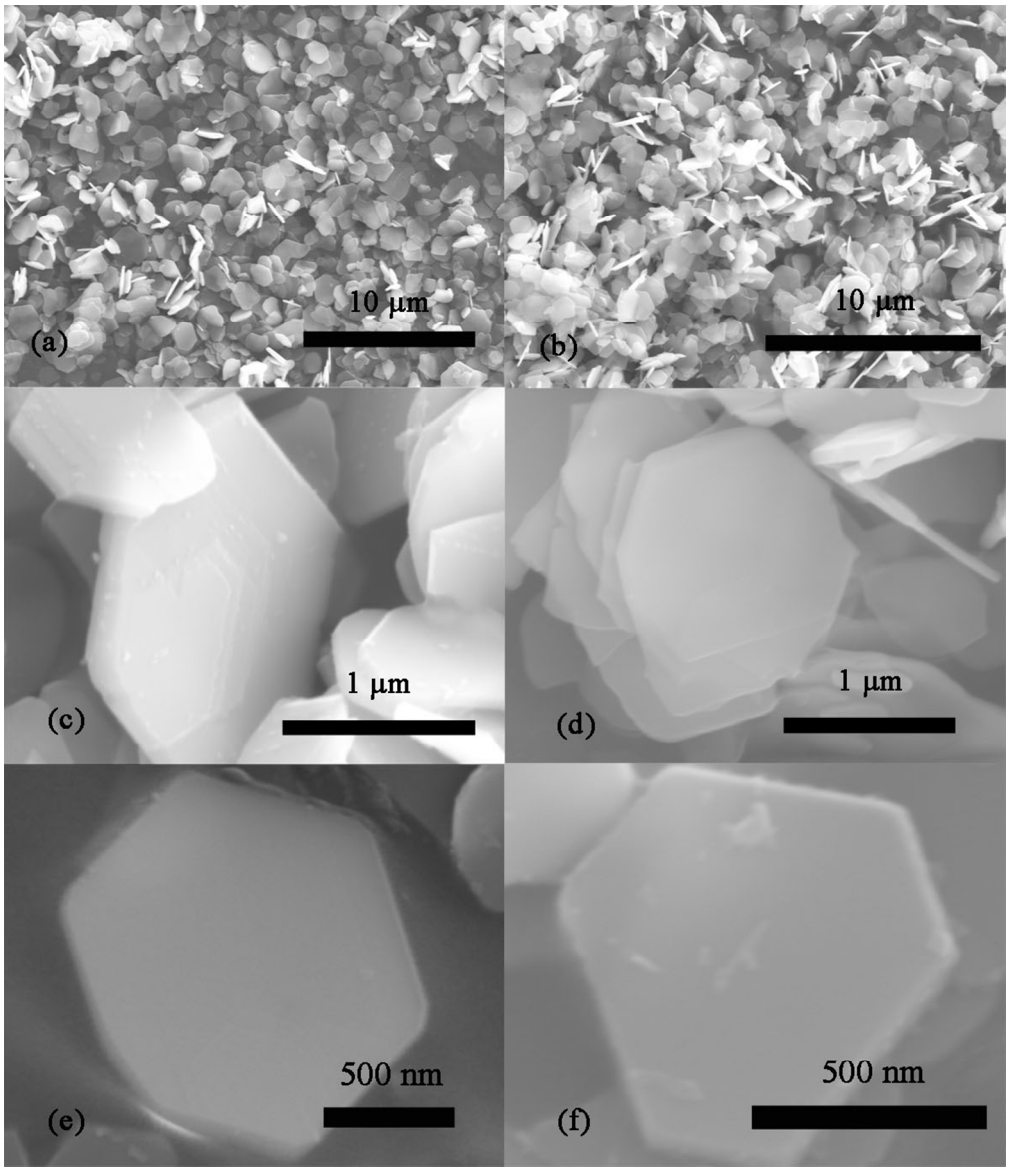

Fig. 2. SEM images of BaFe12O19 (a, c,e) and Zn2+-doped BaFe12O19 (b, d,f) nanoplates.
99x115mm (300 x 300 DPI)

RSC Advances Accepted Manuscript

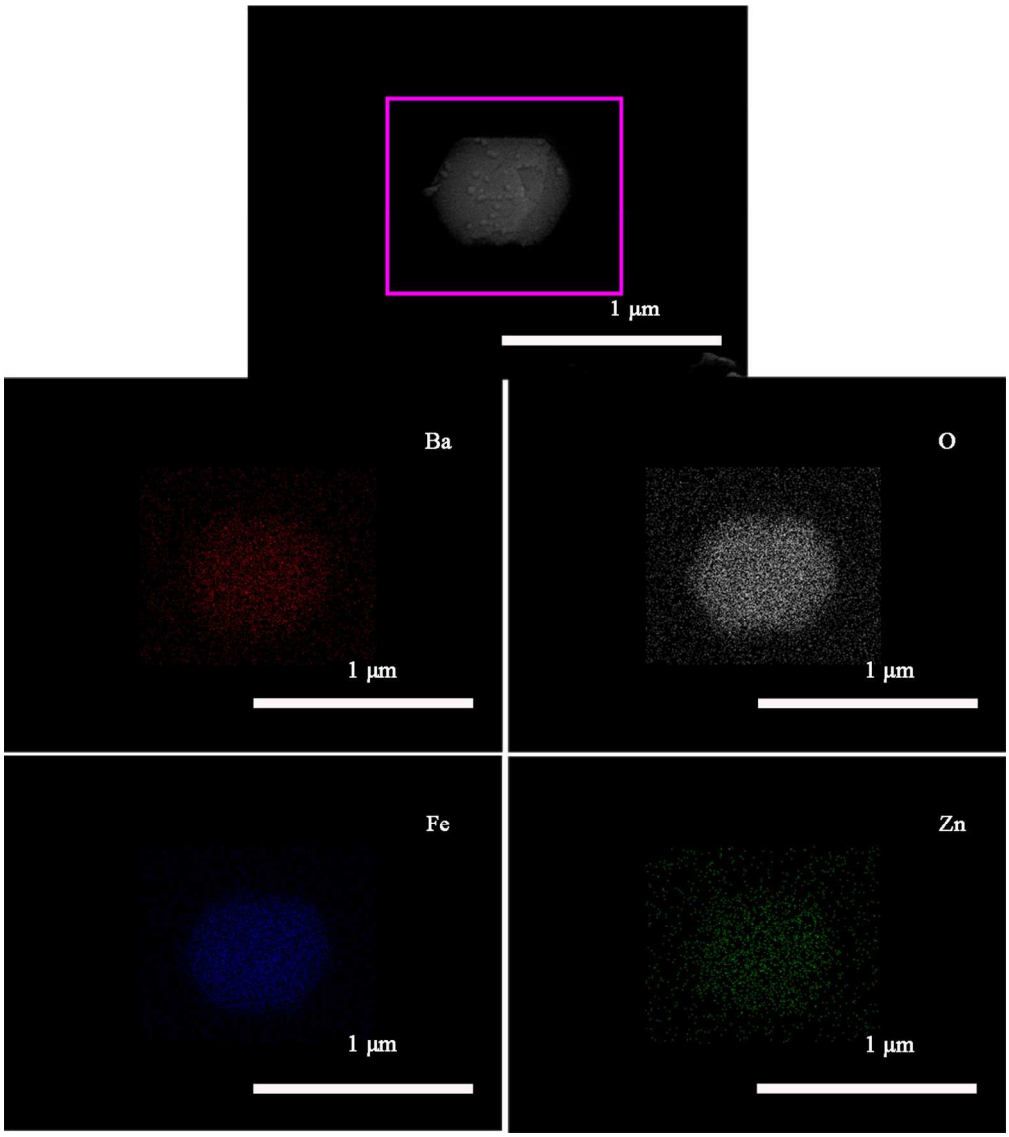

Fig. 3. SEM and EDX mapping images (Fe, O, Ba, Zn) of Zn2+-doped BaFe12O19 nanoplates.
119x135mm (300 x 300 DPI)

RSC Advances Accepted Manuscript

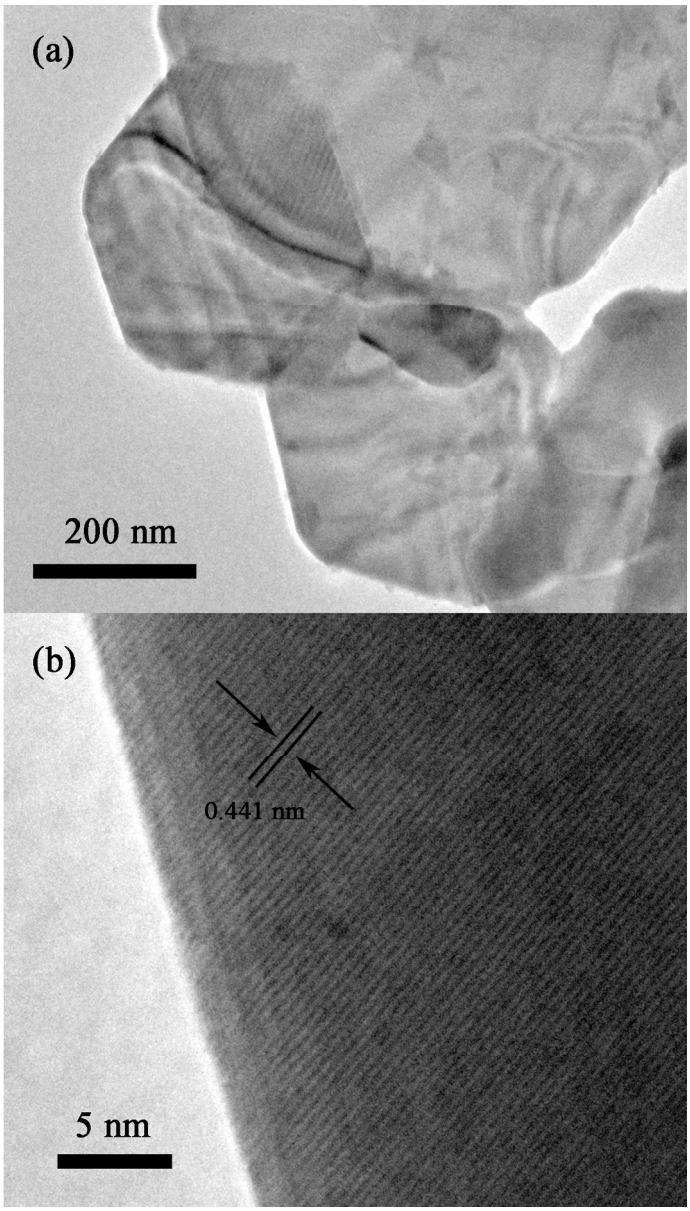

Fig. 4. HR-TEM images of Zn2+-doped BaFe12O19 nanoplates at different magnifications (a, b).
119x210mm (300 x 300 DPI)

RSC Advances Accepted Manuscript

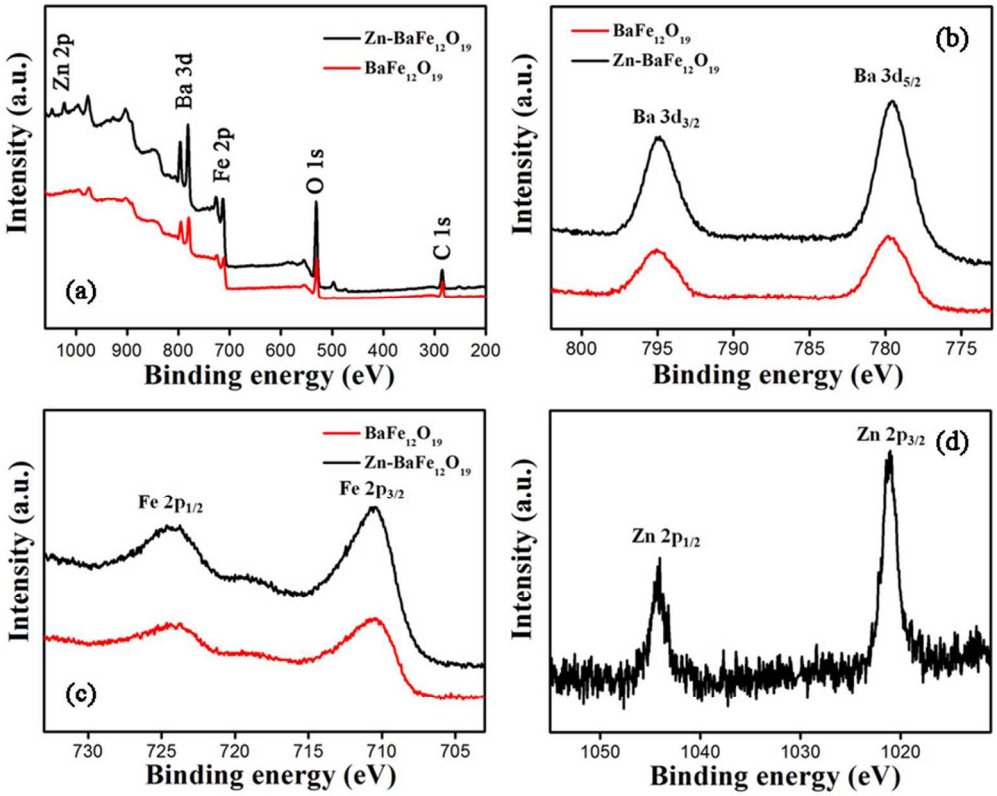

Fig. 5. XPS spectra of (a) survey-scan, (b) Ba 3d, (c) Fe 2p, and (d) Zn 2p of BaFe12O19 and Zn2+-doped BaFe12O19 nanoplates.
80x63mm (300 x 300 DPI)

RSC Advances Accepted Manuscript

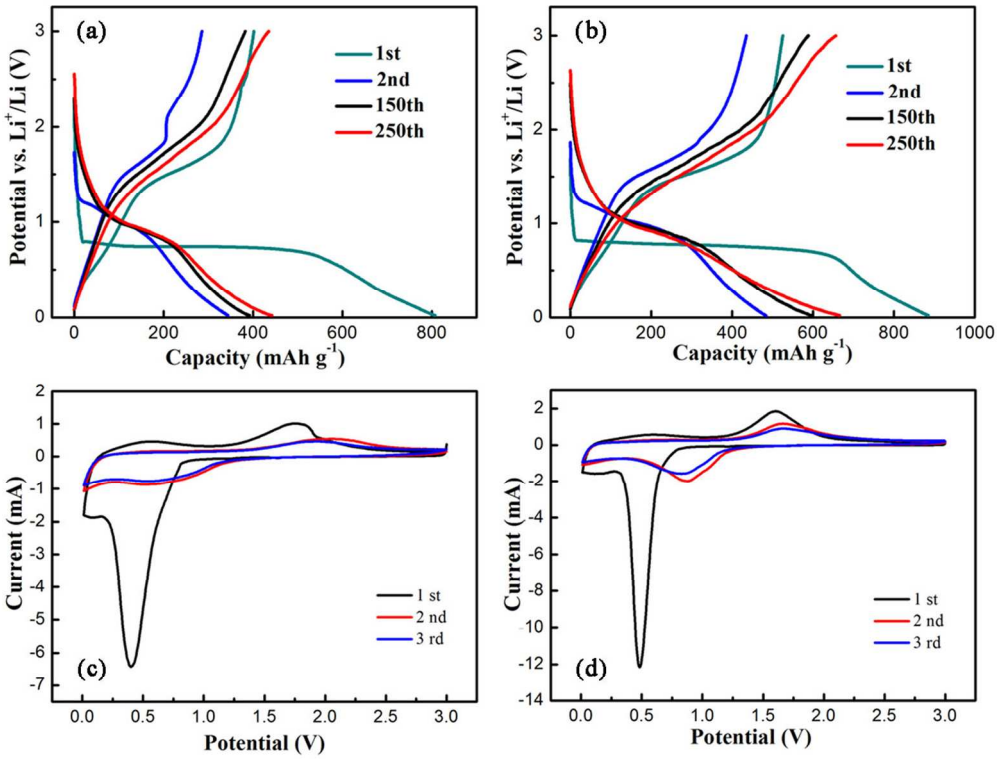

Fig. 6. Galvanostatic discharge/charge curves of the 1st, 2nd, 150th, and 250th cycle for (a) BaFe12O19 and (b) Zn2+-doped BaFe12O19 nanoplates. Cyclic volta voltammograms at a scanning rate of 0.3 mV s-1 between 0.1 and 3.0 V for (c) BaFe12O19 and (d) Zn2+-doped BaFe12O19 nanoplates.
119x92mm (300 x 300 DPI)

RSC Advances Accepted Manuscript

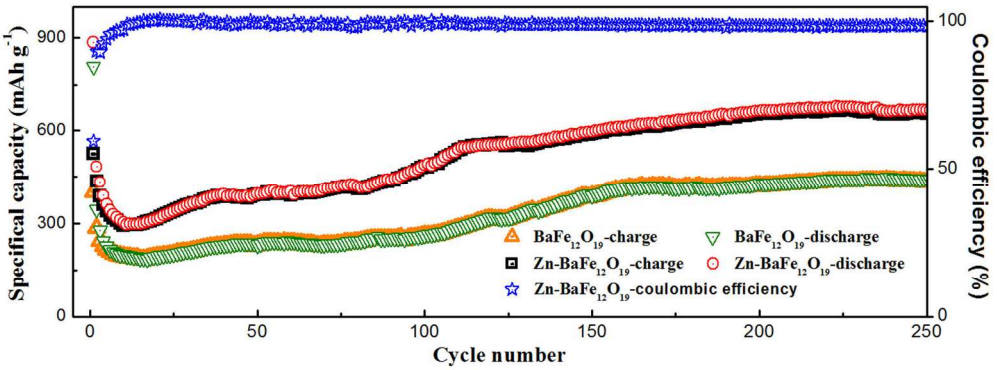

Fig. 7. Cycling performance of BaFe12O19 and Zn2+-doped BaFe12O19 nanoplates at a current density of 100 mA g-1, and columbic efficiency of Zn2+-doped BaFe12O19 nanoplates
160x59mm (300 x 300 DPI)

RSC Advances Accepted Manuscript

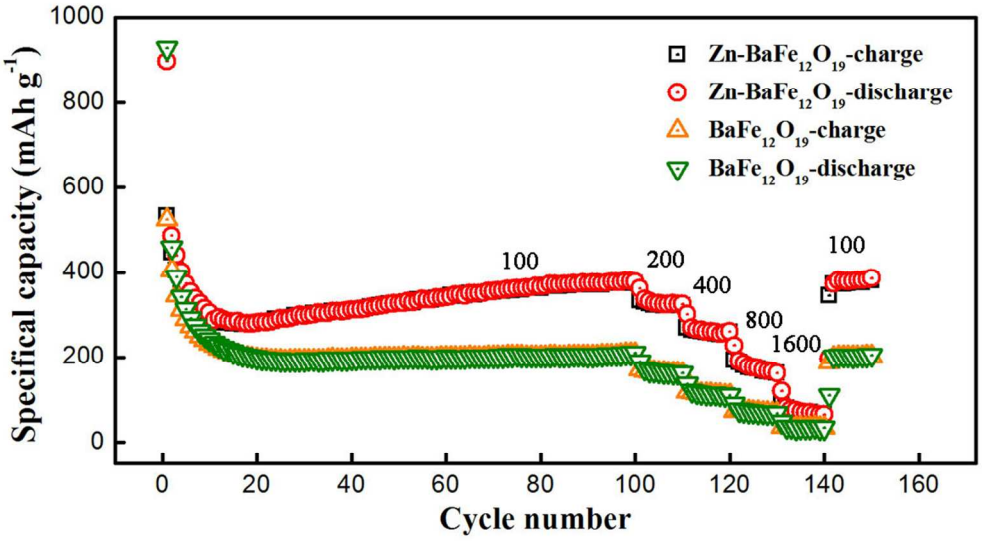

Fig. 8. Discharge and charge capacities of Zn2+-doped BaFe12O19 and BaFe12O19 nanoplates at different cycling rates (from 100 to 1600 mA g-1).
99x54mm (300 x 300 DPI)

RSC Advances Accepted Manuscript

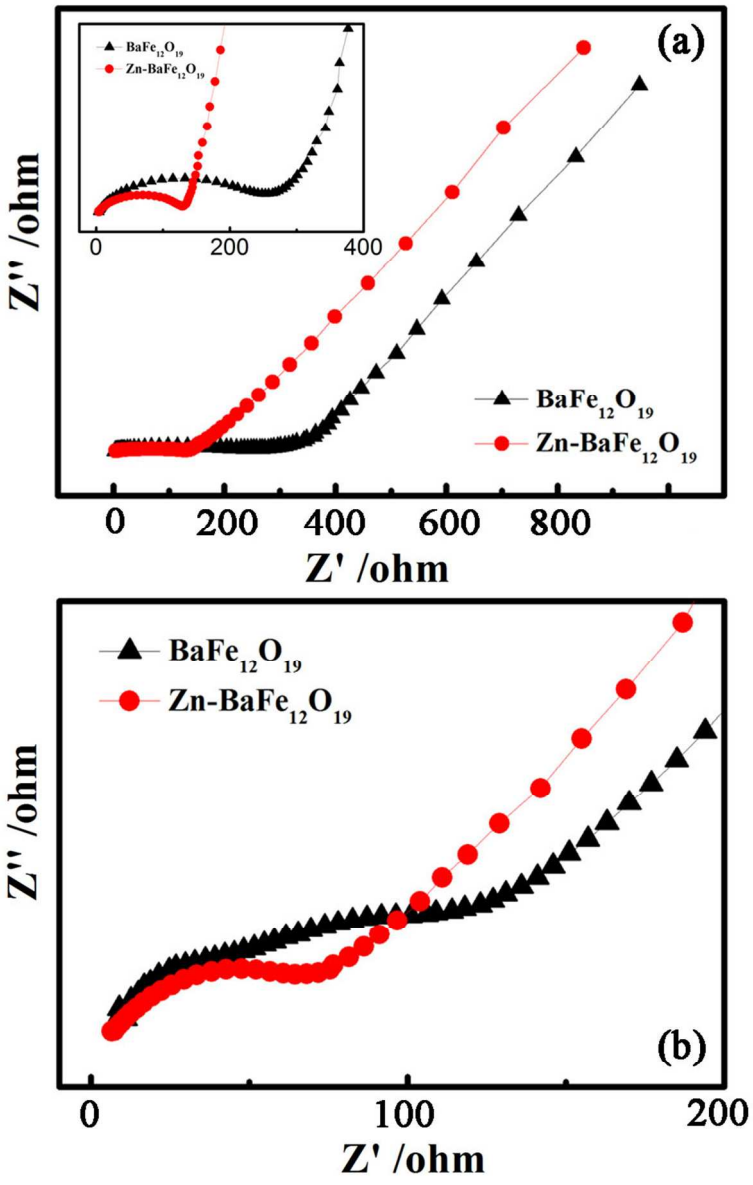

Fig. 9. Nyquist plots of BaFe12O19 and Zn2+-doped BaFe12O19 anodes (a) before discharge/charge process and (b) after 250 cycles.
82x126mm (300 x 300 DPI)

RSC Advances Accepted Manuscript

TOC

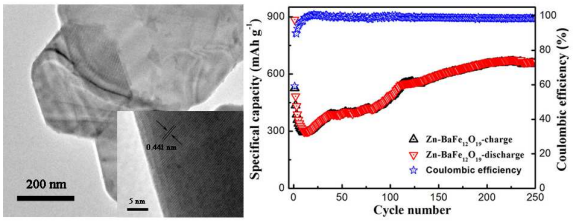

The Zn^{2+}-doped $BaFe_{12}O_{19}$ nanoplates synthesized by a facile approach exhibit superior cycling performances as anode material, attributing to the Zn^{2+} doping.

RSC Advances Accepted Manuscript